

GRB 050713A: HIGH-ENERGY OBSERVATIONS OF THE GAMMA-RAY BURST PROMPT AND AFTERGLOW EMISSION

D. C. MORRIS,¹ J. REEVES,² V. PAL'SHIN,³ M. GARCZARZYK,⁴ A. D. FALCONE,¹ D. N. BURROWS,¹ H. KRIMM,²
N. GALANTE,⁵ M. GAUG,⁶ S. GOLENETSKII,³ S. MIZOBUCHI,⁴ C. PAGANI,¹ A. STAMERRA,⁵ M. TESHIMA,⁴
A. P. BEARDMORE,⁷ O. GODET,⁷ AND N. GEHRELS²

Received 2006 February 21; accepted 2006 August 28

ABSTRACT

Swift discovered GRB 050713A and slewed promptly to begin observing with its narrow-field instruments 72.6 s after the burst onset, while the prompt gamma-ray emission was still detectable in the BAT. Simultaneous emission from two flares is detected in the BAT and XRT. This burst marks just the second time that the BAT and XRT have simultaneously detected emission from a burst and the first time that both instruments have produced a well-sampled, simultaneous data set covering multiple X-ray flares. The temporal rise and decay parameters of the flares are consistent with the internal-shock mechanism. In addition to the *Swift* coverage of GRB 050713A, we report on the *Konus-Wind* (K-W) detection of the prompt emission, an upper limiting GeV measurement of the prompt emission made by the MAGIC imaging atmospheric Cerenkov telescope, and *XMM-Newton* observations of the afterglow. Simultaneous observations with *Swift* XRT and *XMM-Newton* produce consistent results, showing a break in the light curve at $T_0 + \sim 15$ ks. Together, these four observatories provide unusually broad spectral coverage of the prompt emission and detailed X-ray follow-up of the afterglow for 2 weeks after the burst trigger. Simultaneous spectral fits of K-W with BAT and BAT with XRT data indicate that an absorbed broken power law is often a better fit to GRB flares than a simple absorbed power law. These spectral results together with the rapid temporal rise and decay of the flares suggest that flares are produced in internal shocks due to late-time central-engine activity.

Subject headings: gamma rays: bursts

Online material: color figures

1. INTRODUCTION

The *Swift Gamma-Ray Burst Explorer* (Gehrels et al. 2004) has been returning unprecedented data about gamma-ray bursts (GRBs) for the past 18 months. Of particular interest in the bursts followed by *Swift* have been the early-time light curves of the afterglows, which have shown much greater structure and different temporal decay properties than expected, leading to much discussion in the literature regarding the nature of the transition between the prompt emission, thought to be due to synchrotron radiation from internal collisions (Gallant et al. 1999), and the afterglow, also thought to be due to synchrotron radiation, although it remains somewhat unclear whether the emission arises in internal or external shocks. *Swift* observations have shown that GRB light curves can be described by a canonical three-segment shape. This shape consists of (1) an early steep decay phase ($F_\nu \propto \nu^{-\beta} t^{-\alpha}$ where $3 \leq \alpha_1 \leq 5$; $t < 500$ s) (2) a very shallow decay phase ($0.5 \leq \alpha_2 \leq 1.0$; $500 \text{ s} < t < 10^4 \text{ s}$), and (3) a “normal” decay phase ($1 \leq \alpha_3 \leq 1.5$; $10^4 \text{ s} < t$) (Nousek et al. 2006). Superimposed on this smooth decay profile, *Swift* has shown that bright X-ray flares, 2–100 times as bright as the underlying afterglow, are common during the early ($t \leq 10$ ks) stages of GRBs (Burrows et al. 2005b; Falcone et al. 2006; Piro 2005b; Romano et al. 2006).

The observation of GRB 050117 (Hill et al. 2006) marked the first time that *Swift* slewed to and settled on a GRB while the

prompt gamma-ray emission was still in progress, arriving 192 s after the Burst Alert Telescope (BAT) triggered on the burst, which had a T_{90} of 168 s. Due to irregularities in the observing mode of the XRT and the proximity of the South Atlantic Anomaly to *Swift* during the observation of GRB 050117, however, only very sparse data were collected by the XRT, totaling 11.4 s in the first orbit and 946 s overall. This left large gaps in the light curve coverage and severely limited the quality of the spectral analysis that could be performed.

We report here on the observation of GRB 050713A (Falcone et al. 2005), a burst of $T_{90} = 70$ s to which *Swift* slewed and began collecting data with the narrow-field instruments (NFIs) in just 72.6 s, while the prompt gamma-ray emission was still detectable by the BAT. This burst marks just the second time that the BAT and XRT have collected simultaneous data on a burst, and it marks the first time that both instruments have produced a well-sampled, simultaneous data set covering multiple flares in the prompt emission.

In addition to the *Swift* coverage of GRB 050713A, we report also on prompt and follow-up observations carried out by *Konus-Wind*, MAGIC, *XMM-Newton*, and ground-based optical observatories. In § 2 we describe the observations and data analysis from all instruments, including ground follow-up. In § 3 we discuss the implications of the observations in light of the new theoretical understanding emerging from *Swift* observations of GRBs. In § 4 we summarize and present our conclusions. Quoted uncertainties are at the 90% confidence level for one interesting parameter (i.e., $\Delta\chi^2 = 2.71$) unless otherwise noted.

2. OBSERVATIONS AND DATA ANALYSIS

Many different observatories and instruments have observed GRB 050713A. We devote the following section to a description

¹ Department of Astronomy and Astrophysics, Pennsylvania State University, University Park, PA; morris@astro.psu.edu.

² NASA Goddard Space Flight Center, Greenbelt, MD.

³ Ioffe Physico-Technical Institute, Russian Academy of Sciences, St. Petersburg, Russia.

⁴ Max-Planck-Institut für Physik, Munich, Germany.

⁵ Dipartimento di Fisica, Università di Siena, and INFN, Pisa, Italy.

⁶ Institut de Física d'Altes Energies, Barcelona, Spain.

⁷ Department of Physics and Astronomy, University of Leicester, UK.

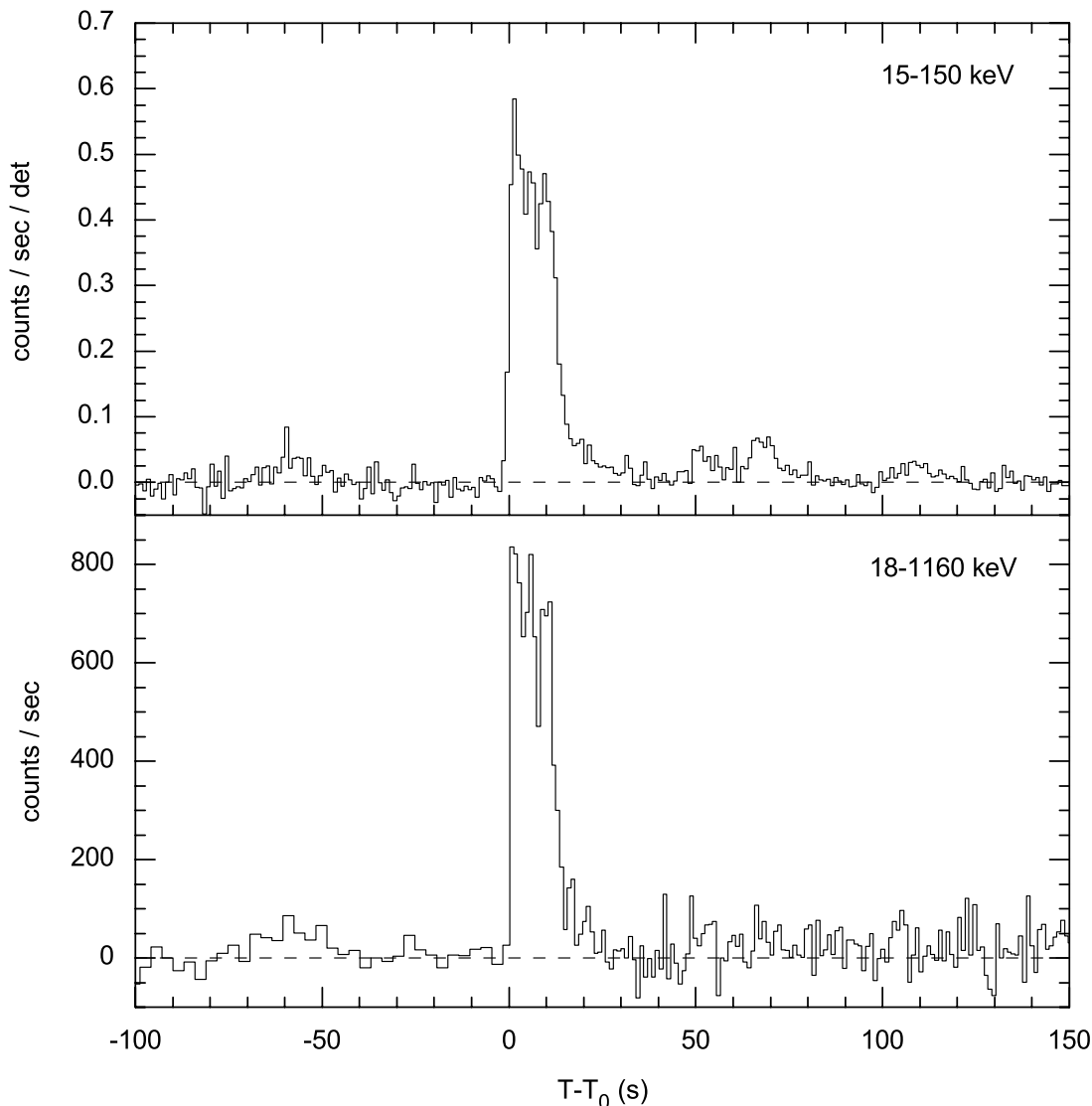


FIG. 1.— Background-subtracted BAT (*top*) and Konus-Wind (*bottom*) light curves on the same timescale. The plots have been adjusted so that the trigger time for both plots is the same relative to the burst. T_0 in the lower plot is $T_0(\text{BAT})$ plus the propagation time between the spacecraft (0.742 s). BAT data are binned to 1 s resolution throughout. K-W data are binned to 2.94 s resolution in survey mode prior to the burst trigger and are binned to 1 s resolution in GRB follow-up mode after the trigger. Note that the precursor at $T_0 - 65$ s is detected in both BAT and K-W while posttrigger flares seen in the BAT at $T_0 + 50$, $T_0 + 65$, and $T_0 + 105$ s are not clearly detected by K-W. This suggests a harder spectrum for the precursor than the posttrigger flares, which is confirmed by joint BAT/K-W spectral fits. The main burst consists of three closely spaced, overlapping pulses in both the BAT and K-W energy ranges. The K-W light curve decays rapidly to background level by $T_0 + 15$ s, while the BAT light curve continues to show low-level emission out to $T_0 + \sim 200$ s.

of the observations and analysis carried out by each instrument team. All spectral fits were performed using XSPEC version 11.3.

2.1. *Swift* BAT

The *Swift* BAT (Barthelmy et al. 2005a) triggered on GRB 050713A at 04:29:02.39 UT, measuring a peak 1 s flux of 6.0 ± 0.4 photons $\text{cm}^{-2} \text{s}^{-1}$. The T_{90} measured in the 15–350 keV energy range is 70 ± 10 s (Palmer et al. 2005). The onset of the burst as defined by the BAT trigger is preceded by a weak, hard (photon index = 1.26) precursor at $T_0 - 60$ s. BAT data were processed using the BAT ground software build 11 and BAT Calibration Database files build 11.

At the time of the BAT trigger, the flux rose rapidly and remained elevated during a 12 s long, multi-peaked burst (Fig. 1). At $T_0 + 12$ s, the BAT flux rapidly decayed with a power-law decay rate of $\alpha \sim 8$ for 5 s before breaking to a more shallow decay

of $\alpha \sim 2.5$ at $T_0 + 17$ s. This decay continued until $T_0 + 40$ s, at which point the BAT flux had decayed to near background levels. At $T_0 + 50$ s, a flare is seen with peak flux 2×10^{-8} ergs $\text{cm}^{-2} \text{s}^{-1}$, extrapolated into the XRT 0.2–10.0 keV bandpass, followed by a flare with peak flux 3.5×10^{-8} ergs $\text{cm}^{-2} \text{s}^{-1}$ at $T_0 + 65$ s, another at $T_0 + 105$ s with peak flux 1×10^{-8} ergs $\text{cm}^{-2} \text{s}^{-1}$, and some hint of further emission at the onset of a flare seen in the XRT at $T_0 + 160$ s. A weak but statistically significant precursor is seen at $T_0 - 70$ to $T_0 - 50$ s, followed by a period of no significant emission from $T_0 - 50$ s to the burst trigger.

The spectrum of the entire BAT data set is well fit by a power-law spectrum with photon index = 1.58 ± 0.07 , although there is evidence for a slightly harder index of 1.45 during the plateau and a softening to $\Gamma = 1.60$ during the rapid decay, and further softening to $\Gamma = 2.0$ during the weak flares. Using the global fit of $\Gamma = 1.58$, the fluence is $(9.1 \pm 0.6) \times 10^{-6}$ ergs cm^{-2} in the 15–350 keV energy range.

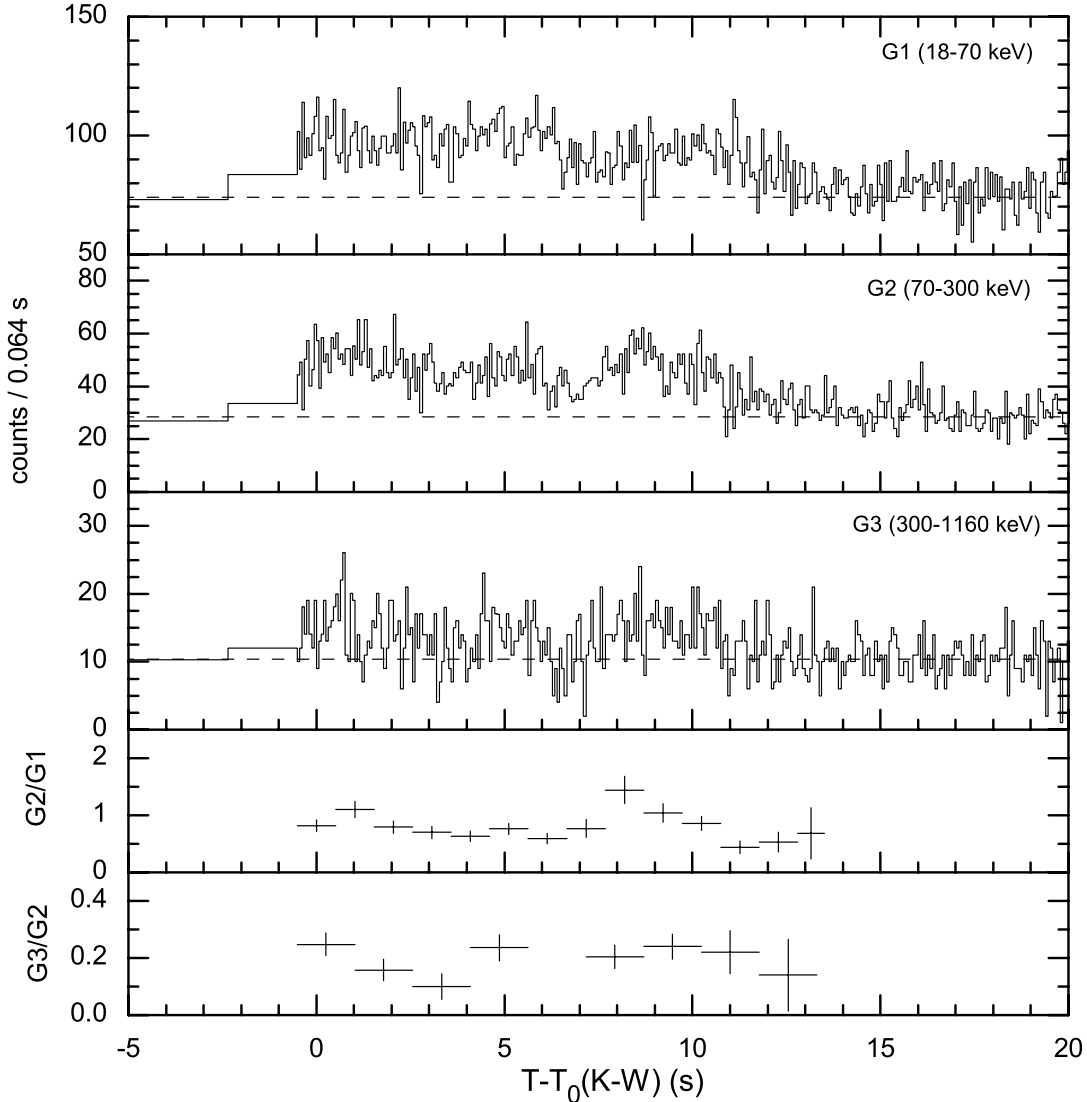


FIG. 2.—Plot of Konus-Wind data in three bands and associated band ratios during burst prompt emission. Data binning is 64 ms.

2.2. Konus-Wind

GRB 050713A triggered Konus-Wind (K-W) (Aptekar et al. 1995) at $T_0(\text{K-W}) = 04:29:01.745$ UT. It was detected by the S2 detector, which observes the north ecliptic hemisphere, with an incident angle of 18.1° . The K-W light curve in three bands is shown in Figure 2. The propagation delay from *Wind* to *Swift* is 1.387 s for this GRB. Correcting for this factor, one sees that the K-W trigger time corresponds to $T_0 + 0.742$ s. Prior to $T_0(\text{K-W}) - 0.512$ s, data were collected by K-W in a survey mode with lower time resolution of 2.944 s and only three broad spectral channels, 18–70, 70–300, and 300–1160 keV. From $T_0(\text{K-W})$ to $T_0(\text{K-W}) + 491.776$ s, 64 spectra in 101 channels were accumulated on timescales varying from 64 ms near the trigger to 8.19 s by the time the signal became undetectable. The multichannel spectra cover the 18 keV to 14 MeV energy range, but no statistically significant emission is seen above 2 MeV. Data were processed using standard Konus-Wind analysis tools.

Joint spectral analysis was carried out using the BAT data between 15 and 150 keV and the KONUS data from 20 to 2000 keV. The spectra were fit by a power-law model with an exponential cutoff: $dN/dE \propto E^{-\alpha} e^{-(2-\alpha)E/E_p}$ where E_p is the peak energy of

the νF_ν spectrum and α is the photon index. The spectrum of the main pulse is well fit (Fig. 3) with photon index $= 1.26 \pm 0.07$ and $E_p = 421^{+119}_{-80}$ keV ($\chi^2 = 138/119$ dof). Joint fits between BAT and Konus were also made for other time intervals, including one which shows the faint precursor detected by both instruments at $T_0 \sim -60$ s, and will be addressed in greater detail in § 3.3.

The main pulse fluence in the 20 keV to 2 MeV range is $8.08^{+0.55}_{-1.77} \times 10^{-6}$ ergs cm^{-2} . The 256 ms peak flux measured from $T_0 + 1.2$ s in the 20 keV to 2 MeV band is $1.34^{+0.11}_{-0.45} \times 10^{-5}$ ergs $\text{cm}^{-2} \text{s}^{-1}$, and the T_{90} durations of the burst in the G1, G2, and G3 energy bands are 17 ± 2 , 14 ± 4 , and 12 ± 2 s, respectively.

2.3. Swift XRT

The XRT (Burrows et al. 2005a) performs an automated sequence of observations (Hill et al. 2004) after *Swift* slews to a GRB detected by the BAT. When the spacecraft first settles on the target, a short image (0.1 s followed by a longer 2.5 s image if a position is not determined in 0.1 s) is taken to determine an accurate position. Following the image, the XRT switches into either Windowed Timing (WT) mode (a high timing accuracy

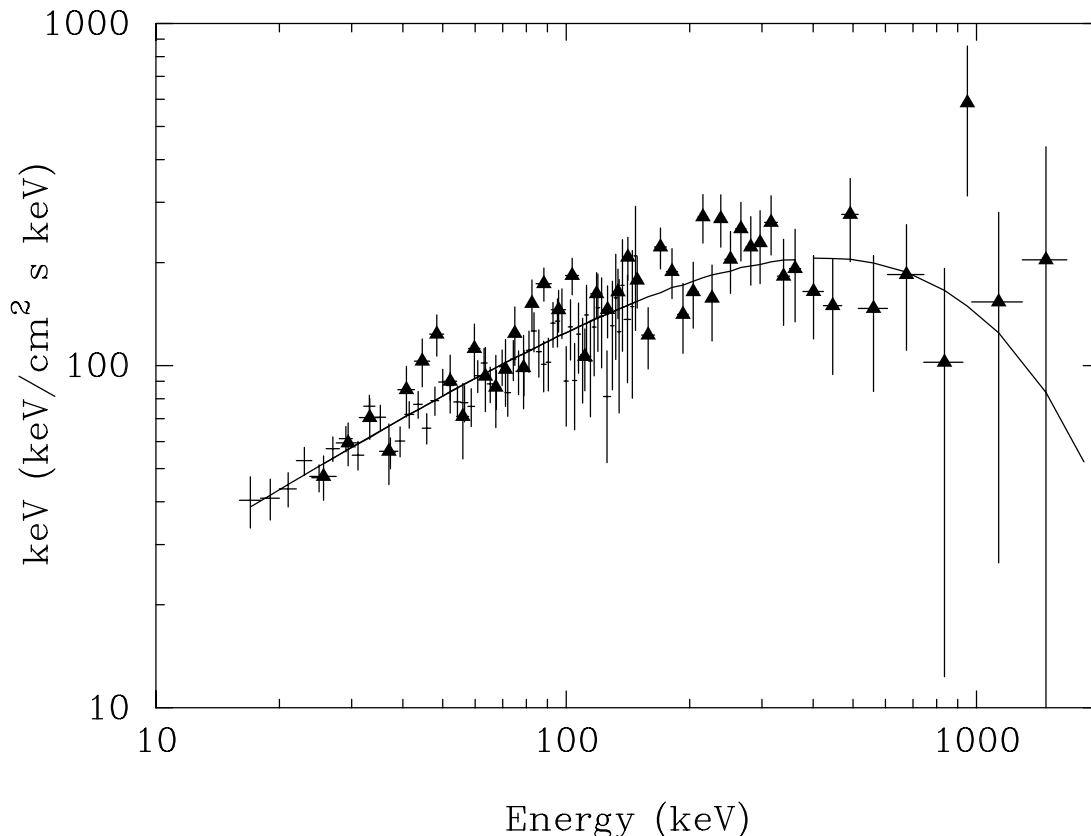


FIG. 3.—Plot of joint SED of Konus-Wind and BAT data during burst prompt emission, showing $E_{\text{peak}} = 421$ keV. Triangles: K-W data. Crosses: BAT data. Data channels have been grouped where appropriate to produce significant data points.

mode with one-dimensional position information) if the source count rate is above 2 counts s^{-1} , or Photon Counting (PC) mode (the more traditional operating mode of X-ray CCDs in which full two-dimensional position information is retained but with only 2.5 s timing resolution) if the count rate is below 2 counts s^{-1} .

XRT collected a 0.1 s Image Mode frame upon settling on GRB 050713A 73 s after the BAT trigger, which yields a count rate of $314 \text{ counts s}^{-1}$. Following the Image Mode frame, XRT cascaded down through its automated mode sequence and collected its first WT frame 4.5 s later. At the onset of the WT data, the XRT count rate was about $100 \text{ counts s}^{-1}$ and decaying as a power law. This initial power-law decay in the XRT WT data, together with the Image Mode data point measured at a flux level ~ 3 times higher just 4.6 s earlier, clearly indicates that the XRT settled and began taking data during the latter portion of the flare detected in the BAT at $T_0 + 65$ s (see Fig. 4). XRT remained in WT mode throughout the entire first orbit of data collection on GRB 050713A, also observing the flare detected by the BAT at $T_0 + 105$ and a lower level flare not clearly detected by the BAT at $T_0 + 155$ s.

Following a 65 minute period of occultation by the Earth, XRT began observations again at $T_0 + 4300$ s, now observing in PC mode since the count rate of the source had decayed below 2 counts s^{-1} . A small flare at $T_0 + 10$ ks and the indication of another flare at $T_0 + 45$ ks are seen in the late-time XRT light curve data, superimposed on an otherwise steady power-law decay. XRT observations continued to monitor the source until $T_0 + 1.8 \times 10^6$ s, a total exposure time of 178 ks, at which time the source had decayed below the XRT detection threshold.

XRT data are processed using the `xrtpipeline` ground software version 0.9.9, the redistribution response matrices `swxwt0to2_`

`20010101v007.rmf` (WT data) and `swxpc0to12_20010101v007.rmf` (PC data), and ancillary response files generated with the `xrtpipeline` task `xrtmkarf`.

2.3.1. XRT GRB Position Analysis

The X-ray afterglow position determined from ground processing of the data is R.A. = $21^{\text{h}}22^{\text{m}}9.8^{\text{s}}$, decl. = $+77^{\circ}4'29.0''$ (J2000.0), with an uncertainty of $3.2''$. This is $10.5''$ from the reported BAT position, $0.5''$ from the optical counterpart reported by Malesani et al. (Malesani et al. 2005), and $1.5''$ from the initial XRT position calculated on board the satellite and automatically distributed via the GCN network (Falcone et al. 2005). An X-ray image compiled from the first segment of XRT PC data is shown as Figure 5 with the BAT, XRT, and optical counterpart error circles displayed. A faint background source is detected $30''$ due south of the GRB afterglow at a constant flux level of $(7 \pm 2) \times 10^{-4} \text{ counts s}^{-1}$. The contribution of this steady source has been removed from the calculation of the afterglow light curve.

2.3.2. XRT Temporal Analysis

A time line of the XRT (as well as other) observations of GRB 050713A is shown in Table 1. The light curve will be broadly treated in two parts. The first part is the initial orbit of data, during which the light curve is characterized by bright flares that are simultaneously observed by the BAT and the K-W instrument at higher energies. Due to the extreme variability in this portion of the light curve, a global decay index cannot be determined from the XRT data. The second part is the remainder of the XRT data from the second orbit onward, which is characterized primarily by a broken-power-law decay, although at least one small flare is seen superimposed atop this global decay.

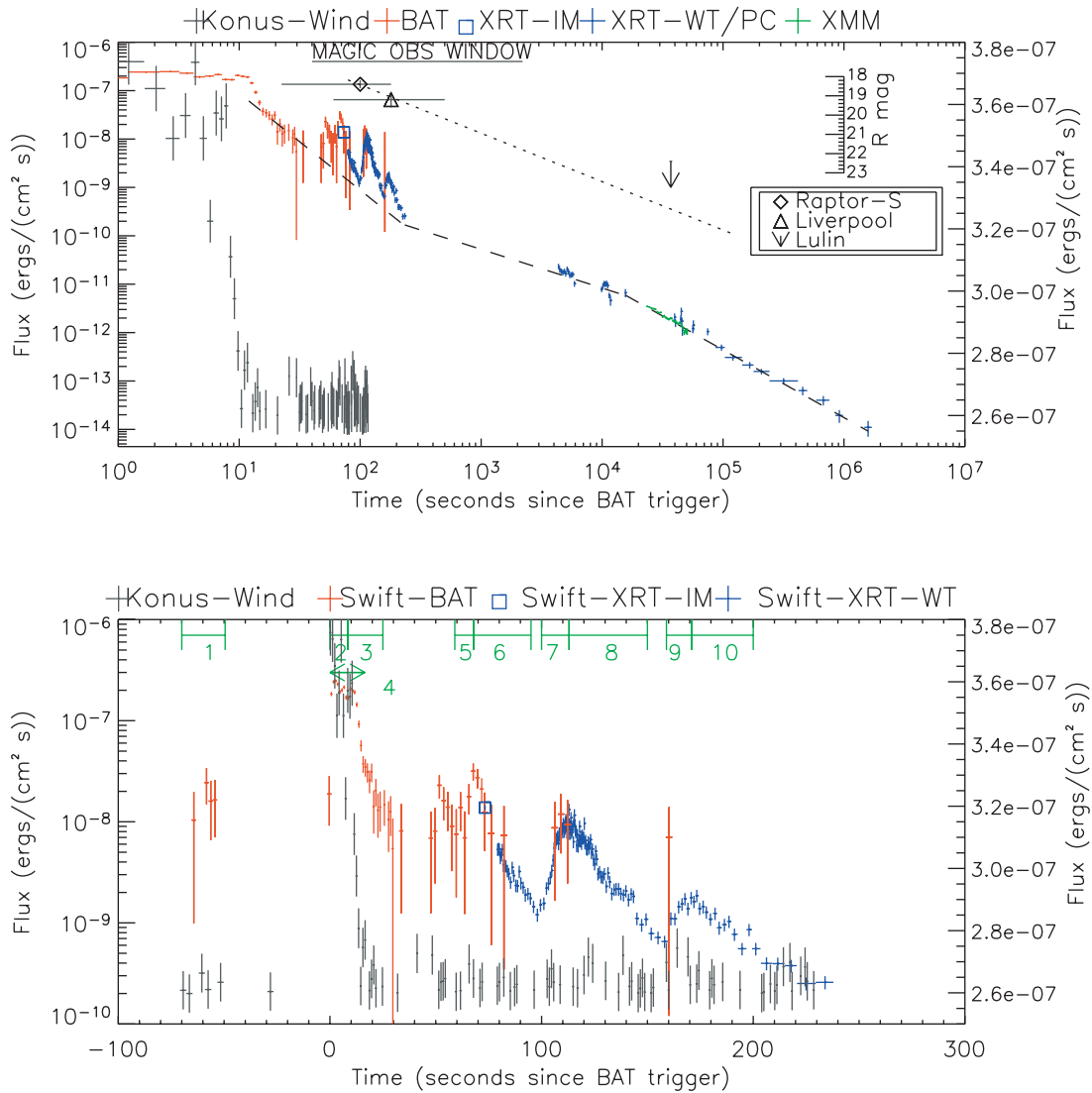


FIG. 4.—X-ray/gamma-ray/optical light curve of GRB 050713A. *Top*: Multicolored points are *Swift* and *XMM* data scaled to the left y-axis. Black crosses are K-W data scaled to the right y-axis. Fluxes are extrapolated into the 0.2–10 keV energy range. The diamond, cross, and arrow are optical observations and scaled to the inset y-axis. The scaling of the inset y-axis is consistent with the outer, left y-axis such that 1 mag is equal to a factor of 2.5 in flux. The window of MAGIC observations is shown by the horizontal bar. The dashed line is the supposed underlying power-law decay. Data from $T_0 + 4$ to $T_0 + 16$ ks are well fit by a flatter power law of slope $t^{-0.8}$, implying an energy-injection phase. A break to a steeper decay of $t^{-1.45}$ occurs at $T_0 + \sim 25$ ks. We note the similar decay slopes in each of the three flares seen by XRT. Optical data are plotted with a fitted power-law decay of $t^{-1.0}$. *Bottom*: A close-up of the flares. Green bars indicate the segments of joint spectral fits.

First orbit.—*Swift* finished slewing to GRB 050713A at $T_0 + 73$ s, during the flare which began at $T_0 + 65$ s. The XRT short image frame is collected just after the peak of this flare, at a flux of 1.2×10^{-8} ergs cm^{-2} s^{-1} , and the first 20 frames of WT data record the decay of the flare. Fitting a simple power law to this decay from $T_0 + 79$ to $T_0 + 100$ s, setting T_0 to be the BAT burst trigger time, we find a power-law index of 5.6 ± 1.8 (1σ). At $T_0 + 105$ s a new flare begins, which rises with a power-law index of 23.3 ± 4.5 for 5–10 s, flattens at the peak of $\sim 9 \times 10^{-9}$ ergs cm^{-2} s^{-1} for 5–10 s, then decays with a more shallow power-law index of 8.4 ± 1.7 for about 30 s. At $T_0 + 165$ s a third flare is detected, which rises with a power-law slope of 8.9 ± 3.1 for 5–10 s, flattens at the peak of $\sim 1.5 \times 10^{-9}$ ergs cm^{-2} s^{-1} for 5–10 s, then decays with a slope of 6.1 ± 1.1 for 70 s before the end of the observing window due to Earth occultation.

Second orbit and later.—The second orbit of data in the XRT is the only single orbit of data in which the afterglow is characterized by a well-sampled (greater than 100 events total) light

curve devoid of any obvious flaring activity. During the 1600 s of data in this orbit, from $T_0 + 4360$ to $T_0 + 5952$ s, the light curve decays steadily as a power law with decay index of about 1.0. The third orbit of data is characterized by another flare, beginning at $T_0 + 10$ ks, lasting throughout the entire orbit (about 2 ks), and reaching a peak flux of 1×10^{-11} ergs cm^{-2} s^{-1} . A power-law fit to the rising portion of the flare yields a slope of 5.8 ± 1.8 , while the decaying portion yields a slope of 11.0 ± 2.5 . This flare seems to be superimposed atop the underlying afterglow decay of decay index $\alpha \sim 1$. Observations were interrupted after 150 s during the fourth orbit due to the occurrence of GRB 050713B, and observations of GRB 050713A remained suspended until $T_0 + 40$ ks. Some suggestion of another flare is seen in the orbit of data beginning at $T_0 + 45$ ks, although the statistics are poor. While afterglow data from the XRT alone do not clearly require a break in the afterglow power law, *XMM-Newton* data (see § 2.4) from $T_0 + 21$ to $T_0 + 50$ ks provide an accurate measure of the late-time decay slope ($\alpha = 1.45$), which cannot fit the XRT data from orbits 2 and 3 without a break in

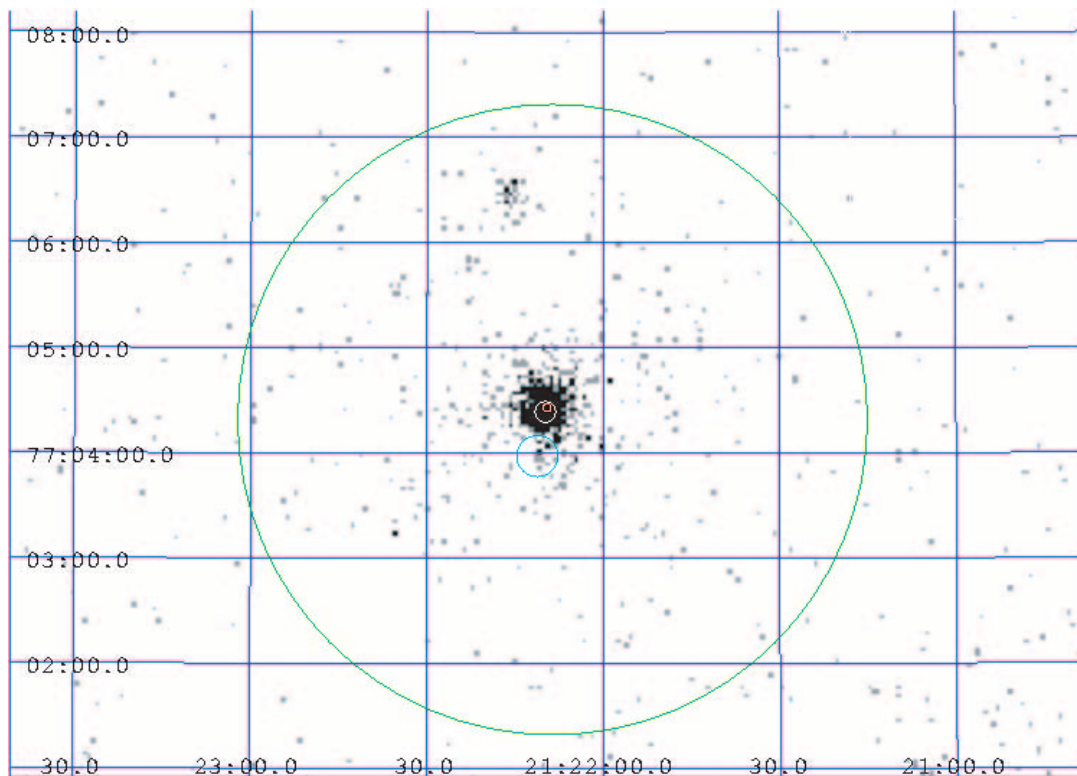


FIG. 5.—XRT image with BAT and XRT optical error circles plotted. Green = BAT, white = XRT, and red = optical. The light blue circle indicates the location of the serendipitous source located $30''$ south of the GRB, which has been subtracted from the data.

the power law. The joint XRT–*XMM-Newton* light curve will be further discussed in § 2.4. Table 2 summarizes the flares and their temporal fits.

2.3.3. XRT Spectral Analysis

The XRT spectral analysis of this burst is somewhat complicated by the high degree of flaring activity seen. In all cases, spectra are binned to a minimum of 20 counts per bin in order to use χ^2 statistics. Fitting the entire first orbit of data, the spectrum is well fit by a highly absorbed power law with photon index = 2.28 ± 0.04 and $N_{\text{H}} = (4.8 \pm 0.2) \times 10^{21} \text{ cm}^{-2}$, which is significantly above the Galactic column ($1.1 \times 10^{21} \text{ cm}^{-2}$) in the direction of GRB 050713A. We are also able, due to the large number of counts in each of the early flares in the data set, to fit a spectrum to both the rising and decaying portions of the flares. In doing so we see the typical hard to soft evolution of the flares (Zhang & Mészáros 2004).

The second orbit of data shows a significantly different spectrum from the first, with a harder spectrum with photon index = 1.9 ± 0.13 and a lower value of $N_{\text{H}} = (3.1 \pm 0.43) \times 10^{21}$, pos-

sibly indicating a period of energy injection (Nousek et al. 2006). The third orbit is well fit by a softer power law similar to that which fit the first orbit with photon index = 2.25 ± 0.23 and $N_{\text{H}} = (4.1 \pm 0.7) \times 10^{21}$.

During the period of overlapping coverage between *Swift* and *XMM-Newton*, XRT has 3.5 ks of exposure time at a mean count rate of $0.04 \text{ counts s}^{-1}$ for a total of about 150 events during the simultaneous observing period. Fitting a spectrum to this overlapping coverage yields a photon index = 1.9 ± 0.30 and $N_{\text{H}} = (4.0 \pm 0.15) \times 10^{21}$. The corresponding mean unabsorbed 0.2–10.0 keV flux during the overlap period as measured by XRT is $(3.4 \pm 0.34) \times 10^{-12} \text{ ergs cm}^{-2} \text{ s}^{-1}$.

The data collected after the third orbit (i.e., after the temporal break in the light curve at $T_0 + \sim 20 \text{ ks}$) are too sparse to justify fitting with higher order models, but a simple absorbed power law fit yields a spectrum of photon index = 2.8 ± 0.6 with $N_{\text{H}} = (5.6 \pm 0.2) \times 10^{21}$. This is consistent with the X-ray photon index found in orbits 1 and 3 and is marginally softer than the photon index found during orbit 2, which as noted above suggests a period of energy injection.

TABLE 1
A SUMMARY OF HIGH-ENERGY OBSERVATIONS OF GRB 050713A

Observatory and Instrument	Start Time (UT)	Stop Time (UT)	Live Time (s)	Time since BAT Trigger (s)
<i>Swift</i> BAT	2005 Jul 13, 04:29:02.4	2005 Jul 13, 04:32:00	178	0
Konus- <i>Wind</i>	2005 Jul 13, 04:29:03.1 ^a	2005 Jul 13, 04:37:14.8	491.8	0.7
MAGIC (limit)	2005 Jul 13, 04:29:42	2005 Jul 13, 05:06:45	2223	40
<i>Swift</i> XRT	2005 Jul 13, 04:30:14	2005 Aug 01, 04:37:02	167740	72
<i>XMM-Newton</i>	2005 Jul 13, 10:17:00	2005 Jul 13, 18:22:00	20900	21000

^a The Konus-*Wind* trigger time corrected for the propagation time from *Wind* to *Swift*.

TABLE 2
GRB 050713A: X-RAY FLARE PARAMETERS

Start Time (s)	Stop Time (s)	Duration (s)	Rise Index α^a	Decay Index α^b	Peak Flux (ergs cm ⁻² s ⁻¹)
79	101	22	NA	5.6 ± 1.8	$3 \times 10^{-8}{}^c$
101	161	60	23.3 ± 5	8.4 ± 1.8	9×10^{-9}
161	304	143	8.9 ± 3	6.1 ± 1.2	1.5×10^{-9}
9751	11840	2089	5.76 ± 1.8	11.0 ± 2.4	1×10^{-11}

^a Index α (unitless) of a power-law fit to the rise of the flare with $T_0 = \text{BAT trigger time}$; $\Gamma_\nu \propto (t - T_0)^\alpha$.

^b Index α (unitless) of a power-law fit to the decay of the flare with $T_0 = \text{BAT trigger time}$; $\Gamma_\nu \propto (t - T_0)^{-\alpha}$.

^c From BAT.

2.4. *XMM-Newton*

XMM-Newton follow-up observations of GRB 050713A commenced at $T_0 + 23.6$ ks (for the EPIC pn) and $T_0 + 20.9$ ks (for the two EPIC MOS cameras). The *XMM-Newton* data were processed with the `epproc` and `emproc` pipeline scripts, using the *XMM-Newton* SAS analysis package, version 6.5. A brightly decaying source is detected near the aim point of all three EPIC detectors, localized at R.A. = $21^{\text{h}}22^{\text{m}}9.4^{\text{s}}$, decl. = $+77^\circ 4' 28.1''$ (J2000.0). The net exposures after screening and dead-time correction are 24.1 ks (pn) and 27.0 ks (MOS). All three EPIC cameras (pn and two MOS) were used in Full Window Mode with the medium filter in place.

Source spectra and light curves for all three EPIC cameras were extracted from circular regions of $20''$ radius centered on the afterglow. Background data were taken from a $60''$ circle on the same chip as the afterglow, but free of any X-ray sources. Fitting the afterglow light curve with a simple-power-law decay results in a decay index of $\alpha = 1.45 \pm 0.05$. Several flares are present in the background light curve, so as a conservative check, we

also excluded times where the background rate is >0.1 counts s⁻¹. The afterglow decay rate is then $\alpha = 1.39 \pm 0.09$, consistent with the above value. The decay rate from the MOS light curve (for the two detectors combined) is also consistent at $\alpha = 1.35 \pm 0.06$.

2.4.1. *XMM-Newton* Spectral Analysis

Afterglow and background spectra were extracted with the same regions used for the light curves, while ancillary and redistribution response files were generated with the SAS tasks `arfgen` and `rmfgen`, respectively. As with XRT data, source spectra were binned to a minimum of 20 counts per bin in order to use χ^2 statistics. The pn and MOS spectra were fitted jointly, allowing only the cross normalization to vary between the detectors, which is consistent within $<5\%$. The two MOS spectra and responses were combined to maximize the signal-to-noise ratio, after first checking that they were consistent with each other. The average net source count rates obtained over the whole observation are 0.58 ± 0.01 counts s⁻¹ for the pn and 0.20 ± 0.01 counts s⁻¹ per MOS module.

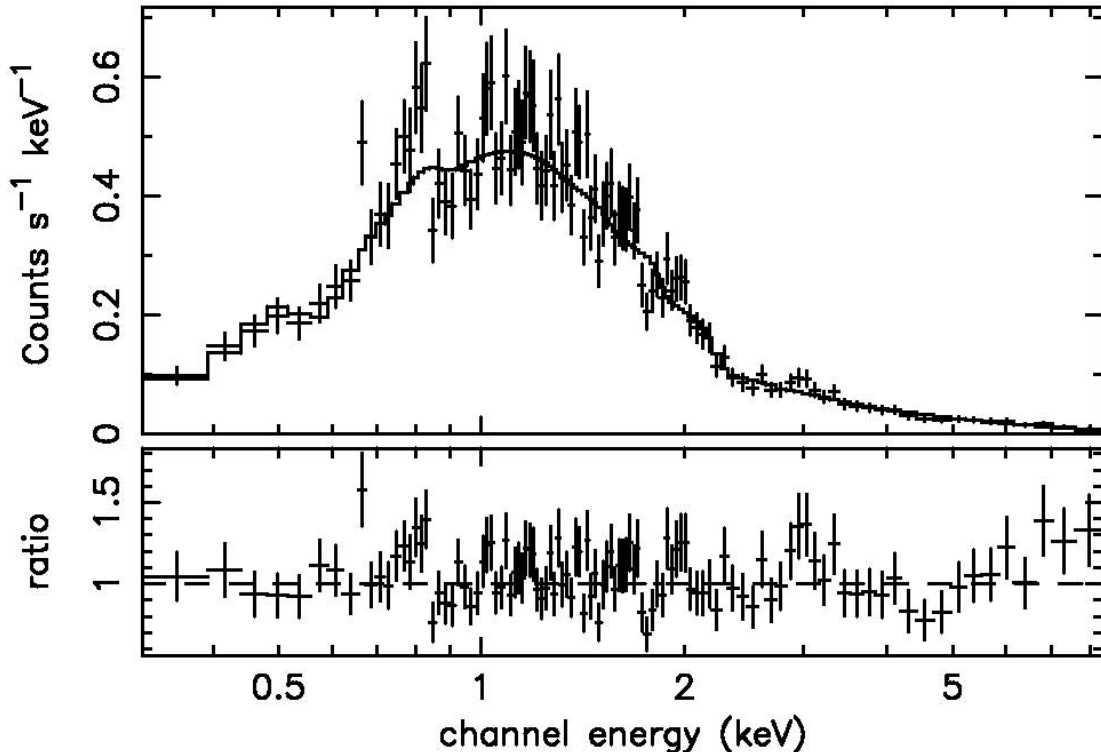


FIG. 6.—PN spectrum from the first 8 ks of the *XMM-Newton* observation. The top panel shows the PN data (*crosses*) with best-fit model (*solid line*) overlaid, which consists of an absorbed power law with photon index = 2.07 and $N_{\text{H}} = 3.2 \times 10^{21}$ cm⁻². The bottom panel shows the data/model ratio residuals to this continuum model. A weak excess of counts is seen near 0.8 and 3 keV, although if interpreted as emission lines, the detection is not significant.

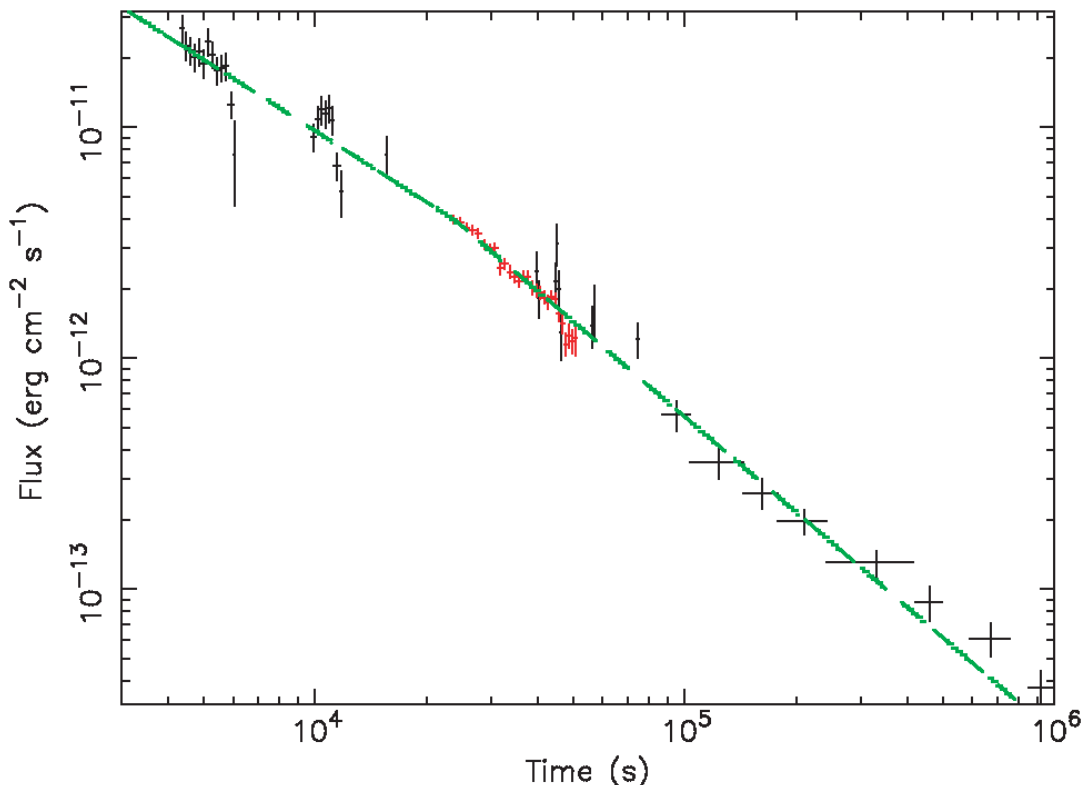


FIG. 7.— Joint *Swift* XRT and *XMM-Newton* PN light curve. *Swift* data are from $T_0 + 4$ to $T_0 + 1000$ ks. *Swift* XRT points are shown in black and *XMM-Newton* in red. The afterglow flux is measured in the 0.5–10 keV band, not correcting for absorption. The solid line plotted to the different segments of data is a broken-power-law decay model, outlined in the text. The *XMM-Newton* decay index ($\alpha = 1.45$) is considerably steeper than in the XRT at earlier times ($\alpha = 1.0$), suggesting that a break occurs in the light curve decay at around $T_0 + 25$ ks.

Allowing the absorption column to vary in the spectral fit results in a formally acceptable fit ($\chi^2/\text{dof} = 515/496$). The N_{H} value obtained is $(3.1 \pm 0.1) \times 10^{21} \text{ cm}^{-2}$, while the continuum photon index = 2.07 ± 0.04 . The time-averaged, unabsorbed, 0.2–10.0 keV flux obtained for the afterglow is $3.2 \times 10^{-12} \text{ ergs cm}^{-2} \text{ s}^{-1}$. These values are consistent with the *Swift* XRT measurement obtained at the time of the *XMM-Newton* observation.

The *XMM-Newton* afterglow spectra were also sliced into three segments of approximately 8 ks in length, in order to search for any spectral evolution within the *XMM-Newton* observation. No change in the continuum parameters was found, all three spectral segments being consistent with photon index = 2.1 and $N_{\text{H}} = 3 \times 10^{21} \text{ cm}^{-2}$. The spectrum obtained from the pn detector and residuals to an absorbed-power-law model (with $\Gamma = 2.08 \pm 0.02$ and $N_{\text{H}} = 3.2 \times 10^{21} \text{ cm}^{-2}$) are shown in Figure 6.

2.4.2. Joint *XMM-Newton* and *Swift* Modeling of the Late-Time Afterglow

The power-law decay index obtained from the *XMM-Newton* observation ($\alpha = 1.4$) appears to be steeper than that obtained from the *Swift* XRT in orbit 2 ($\alpha = 1.0$). In order to compare between the *XMM-Newton* and *Swift* afterglow light curves, a combined light curve from the *XMM-Newton* and *Swift* observations was produced, scaling to the absorbed continuum fluxes measured in the 0.5–10 keV band. The joint *Swift* and *XMM-Newton* light curve is shown in Figure 7, zoomed to better display the region at which the light-curve break occurs.

A single-power-law decay slope of $\alpha = 1.20 \pm 0.02$ is an extremely poor fit to the light curve in this region, with a fit statistic of $\chi^2/\text{dof} = 201.2/65$. Indeed, the light curve from $T_0 + 4$ until $T_0 + 1000$ ks can be better fitted with a broken power law. There

is a flat decay index of $\alpha = 1.02 \pm 0.07$ at early times and a steeper decay index of $\alpha = 1.45 \pm 0.06$ at later times, with the break in the decay occurring at $T_0 + 25 \pm 3$ ks. The fit statistic is then $\chi^2/\text{dof} = 90.2/59$. The remaining contribution toward the χ^2 originates from two small possible flares present near $T_0 + \sim 10$ and $T_0 + \sim 45$ ks.

2.5. MAGIC

The MAGIC (Major Atmospheric Gamma Imaging Cherenkov) Telescope (Mirzoyan et al. 2005) was able to observe part of the prompt-emission phase of GRB 050713A as a response to the alert provided by *Swift*. The observation, at energies above 175 GeV, started at $T_0 + 40$ s, 20 s after reception of the alert. It overlapped with the prompt-emission phase measured by *Swift* and K-W, and lasted for 37 minutes, until twilight. The observation window covered by MAGIC did not, however, contain the burst-onset peak detected at keV–MeV energies, where the *Swift* and K-W spectra were taken. The same region of the sky was observed 48 hr after the burst onset, collecting an additional 49 minutes of data, which was used to determine the background contamination.

The MAGIC Telescope is currently the largest single-dish imaging air Cerenkov telescope (IACT) in operation, with the lowest energy threshold (60 GeV at zenith, increasing with zenith angle). In its fast slewing mode, the telescope can be repositioned within ~ 30 s. In case of an alert by GCN, an automated procedure takes only a few seconds to terminate any pending observation, validate the incoming signal, and start slewing toward the GRB position, as was the case for GRB 050713A.

Using the standard analysis, no significant excess of gamma-like air showers from the position of GRB 050713A above 175 GeV was detected (Albert et al. 2006). This holds both for the prompt

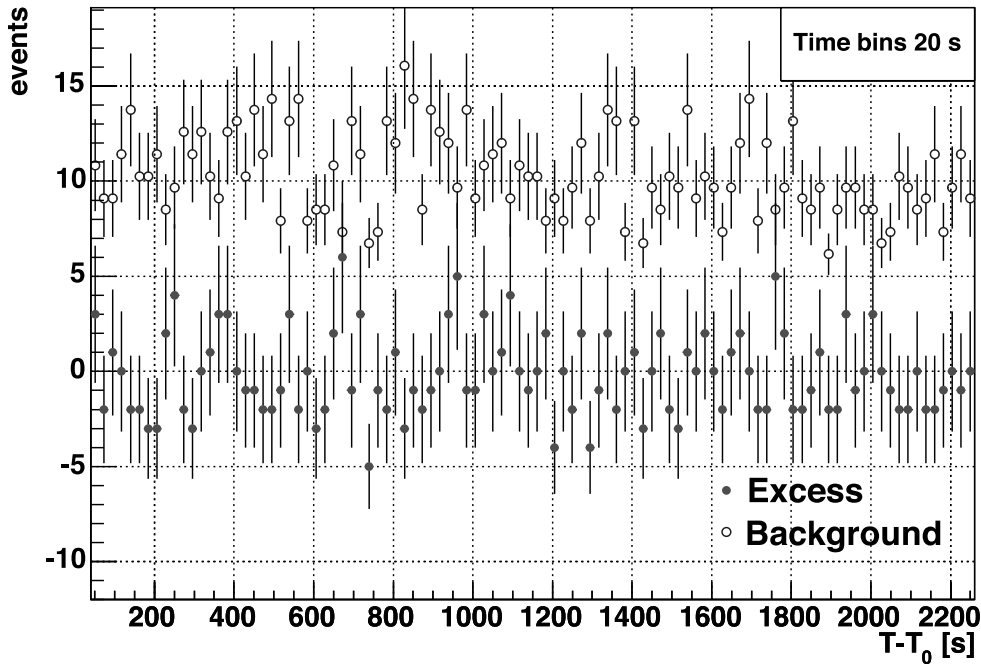


FIG. 8.—MAGIC observations. *Filled circles*: Number of excess events for 20 s intervals, in the 37 minute window after the burst onset. *Open circles*: Number of background events in the signal region. No significant source signal is detected above the background. [See the electronic edition of the Journal for a color version of this figure.]

emission and during the subsequent observation periods. Figure 8 shows the number of excess events during the first 37 minutes after the burst, in intervals of 20 s. For comparison, the number of expected background events in the signal region, stable and compatible with statistical fluctuations, is shown. Upper limits to the gamma-ray flux are given in Table 3. This is the first observation of the GRB prompt-emission phase performed by an IACT.

2.6. Optical and Other Follow-Up Observations

Optical follow-up observations of GRB 050713A performed by the UVOT and by ground-based observatories are summarized in Table 4.

The earliest optical afterglow measurement comes from the RAPTOR-S robotic telescope at the Los Alamos National Laboratory in Los Alamos, New Mexico, at $R = 18.4 \pm 0.18$ in a co-added series of 8×10 s images with a midpoint observation time of $T_0 + 99.3$ s (Wren et al. 2005). A nearly simultaneous measurement was made by the robotic Liverpool Telescope in a co-added series of three ~ 2 minute exposures in the r' band with a

midpoint of observation of $T_0 + 3$ minutes (Malesani et al. 2005). Later detections below the Digitized Sky Survey limits were reported within the first 60 minutes after the burst trigger in the R band by the Nordic Optical Telescope ($T_0 + 47$ minutes), in the I band by the Galileo Italian National Telescope in the Canary Islands, and in the infrared J , H , and K bands by the Astronomical Research Consortium Telescope at Apache Point Observatory ($T_0 + 53$ minutes).

Due to the bright ($V = 6.56$) star HD 204408, which is located just $68''$ from the position of the burst, the UVOT background level at the position of the afterglow is significantly higher than usual, resulting in abnormally poor sensitivity of the instrument in detecting the afterglow of GRB 050713A. Considering this high background, the nondetection of the afterglow by the UVOT is not surprising.

All other reported optical observations of the afterglow position have yielded only upper limits. Most of the upper limits are near in time to the actual detections but at brighter magnitudes and thus do not produce strong constraints on the decay rate of the optical afterglow. The R -band measurement made at $T_0 + 10.3$ hr by the Lulin Telescope in Taiwan, however, is at a sufficiently late epoch to place a useful constraint on the optical decay rate. Fitting a simple power law to the two well-defined measurements at $T_0 + 99.3$ and $T_0 + 180$ s and the upper limit at $T_0 + 10.3$ hr yields an upper limit on the power-law decay slope of $\alpha \geq 0.5$, as shown in Figure 4.

A radio follow-up observation made with the VLA reports no detection at $T_0 + 4.3$ days.

3. DISCUSSION

3.1. Multispectral Light Curve Overview

The K-W light curve in the 18–1160 keV energy range is similar to the *Swift* BAT light curve (Fig. 1). The small precursor

TABLE 3
MAGIC UPPER LIMITS ON GRB 050713A

ENERGY (GeV)	EXCESS EVENTS (UPPER LIMITS)	EFFECTIVE AREA ($\times 10^8$ cm 2)	FLUX LIMITS	
			cm $^{-2}$ keV $^{-1}$ s $^{-1}$	crab
175–225.....	8.5	1.7	1.3×10^{-17}	7.6
225–300.....	10.4	3.4	3.9×10^{-18}	4.8
300–400.....	6.0	5.3	1.6×10^{-18}	3.8
400–1000....	4.3	6.5	2.3×10^{-19}	3.3

NOTES.—MAGIC upper limits (95% CL) on GRB 050713A between $T_0 + 40$ and $T_0 + 130$ s. Limits include a systematic uncertainty of 30%. The crab unit = $1.5 \times 10^{-6} \times (E/\text{GeV})^{-2.58}$ photons cm $^{-2}$ s $^{-1}$ GeV $^{-1}$.

TABLE 4
GRB 050713A: GROUND-BASED OPTICAL AND RADIO FOLLOW-UP

Observatory	Time	Band	Magnitude/Limit
McDonald Observatory, Texas	$T_0 + 22.4$ s	Unfiltered	17.7 (limit)
RAPTOR-S, LANL	$T_0 + 99.3$ s	<i>R</i>	18.4 ± 0.18
Liverpool Robotic Telescope, Canary Islands	$T_0 + 180$ s	<i>r'</i>	19.2
<i>Swift</i>	$T_0 + 252$ s	<i>V</i>	17.98
	$T_0 + 309$ s	<i>U</i>	17.81
	$T_0 + 311$ s	UVM2	17.13
	$T_0 + 325$ s	UVW1	16.85
	$T_0 + 326$ s	UVW2	17.08
	$T_0 + 351$ s	<i>B</i>	18.08
Red Buttes Observatory, Wyoming.....	$T_0 + 27$ minutes	<i>R</i>	19.4 (limit)
	$T_0 + 31$ minutes	<i>I</i>	18.2 (limit)
Nordic Optical Telescope	$T_0 + 47$ minutes	<i>R</i>	< DSS limit
Galileo National Telescope, Canary Islands	$T_0 + 48$ minutes	<i>I</i>	< DSS limit
ARC Telescope, Apache Point Observatory	$T_0 + 53$ minutes	<i>J, H, K</i>	Detected
Red Buttes Observatory, Wyoming.....	$T_0 + 93$ minutes	<i>R</i>	19.4 (limit)
	$T_0 + 98$ minutes	<i>I</i>	18.7 (limit)
Lulin Telescope, Taiwan.....	$T_0 + 10.3$ hr	<i>R</i>	22.4 (limit)
VLA, NRAO.....	$T_0 + 4.3$ days	8.5 GHz	96 μ Jy

peak detected by BAT at $T_0 - 70$ to $T_0 - 50$ s is seen by K-W at statistically significant levels in all three broad, pretrigger bands: G1 (18–70 keV), G2 (70–300 keV), and G3 (300–1160 keV). The other smaller peaks detected by the BAT after the burst trigger are not seen at statistically significant levels in the K-W data, despite the fact that the peaks at $T_0 + 50$ and $T_0 + 65$ s are more intense in the BAT energy range than the precursor is. The detection by K-W of the precursor but not the later flares is indicative of the harder spectral index seen in the precursor as compared to the later flares (see § 3.3 for discussion of separate spectral fits to individual flares).

The XRT light curve with BAT data overplotted is shown in Figure 4. Both the X-ray and gamma-ray data in the first orbit are dominated by flaring activity, making it difficult to draw a conclusion regarding the underlying power-law decay index from this orbit alone. The XRT data beginning at $T_0 + 4$ ks (orbit 2) and extending until $T_0 + 40$ ks show a significantly flatter power-law decay slope of $\alpha = -0.8$, implying that a break in the power-law decay has occurred near the end of the first orbit of XRT coverage at $T_0 + \sim 300$ s and that a period of energy injection occurs from $T_0 + \sim 300$ s to $T_0 + \sim 15$ ks. Another break in the light curve then occurs near $T_0 + 25$ ks to a steeper, “normal,” pre-jet-break decay slope, as shown by the *XMM-Newton* data ($\alpha \sim 1.4$). Support for this notion of the presence of an energy-injection phase may be drawn from the harder X-ray spectral slope of the second orbit of XRT data (photon index = 1.9 ± 0.13) compared to the first orbit (photon index = 2.28 ± 0.04), the third orbit (photon index = 2.25 ± 0.23), and the later data (photon index = 2.8 ± 0.6) (Table 5). *XMM-Newton* data cover-

age nicely fills much of the data gap in the XRT coverage between $T_0 + 15$ and $T_0 + 40$ ks and provides high signal-to-noise data in this regime, producing a confident determination of the light curve break.

The global picture of the light curve of this burst is one in which the early data (prior to $T_0 + 12$ s) show a bright plateau in the 15 keV to 1 MeV energy range, consisting of multiple overlapping peaks. At $T_0 + 12$ s the emission drops rapidly, consistent with a curvature radiation falloff (Zhang et al. 2006) until subsequent flaring activity begins to be seen in the 0.3–150 keV region with some indication of flux at higher energies from K-W. Due to the rapid rise and decay of the flares, internal shocks from continued central-engine activity appear to be the most likely explanation for these flares (Ioka et al. 2005). The earliest ground-based optical detections are reported at this time also, suggesting that the flares may also be optically bright. The lack of higher resolution timing information in the optical data, however, admits the possibility that the optical emission may be unassociated with the emission mechanism responsible for the X-ray flares. It is possible that the optical emission is due to synchrotron emission from the reverse shock (RS), although the much higher flux level of the X-ray flare peaks compared to the optical measurements suggests that the X-ray flares themselves are not due to inverse Compton scattering of the optical synchrotron emission of the RS (Kobayashi et al. 2007; Gendre et al. 2007).

Following this prompt-emission phase, an energy-injection phase begins that dominates the light curve until at least $T_0 + 16$ ks. During the energy-injection phase, continued activity of the central engine adds energy to the afterglow of the burst, either through

TABLE 5
Swift AND *XMM-Newton* SPECTRAL FITS PREBREAK AND POSTBREAK

Observatory	Photon Index	N_{H} (cm^{-2})	Comment
<i>Swift</i> orbit 1	2.28 ± 0.04	$(4.8 \pm 0.2) \times 10^{21}$	Pre-energy-injection phase
<i>Swift</i> orbit 2	1.90 ± 0.13	$(3.1 \pm 0.4) \times 10^{21}$	Energy-injection phase
<i>Swift</i> orbit 3	2.25 ± 0.23	$(4.1 \pm 0.7) \times 10^{21}$	Flare during energy injection
<i>Swift</i> after orbit 3.....	2.8 ± 0.6	$(5.6 \pm 0.2) \times 10^{21}$	Postbreak
<i>XMM-Newton</i>	2.1 ± 0.05	$(3.0 \pm 0.1) \times 10^{21}$	Postbreak

additional ejection events or through the realization of energy contained in previously ejected outward-moving relativistic shells that only collide at later times, producing late-time internal-shock emission that is then added to the overall decay (Zhang et al. 2006). It may be expected, if the energy-injection phase is due to continued central-engine activity, that flaring behavior would continue to be observed during this period, and indeed, some evidence for small-scale flaring activity during both the second and third orbit of XRT data can be seen, although at a much reduced significance in comparison to the flaring activity of the first orbit. Near $T_0 + 25$ ks, the energy-injection phase ends, giving way to a steeper decay slope similar to what is often seen in GRBs after the prompt-emission phase and prior to the possible onset of a traditional jet break (Nousek et al. 2006).

3.2. Flares

Many flares superimposed on top of the overall decay of GRB 050713A show the typical properties seen in other bursts: that $\delta t/t \sim 0.1$ and that the peak flux level is negatively correlated with the time of the flare (Falcone et al. 2006; Barthelmy et al. 2005b). These two properties of flares seen in *Swift* GRB afterglows have been cited as evidence for flares being produced through accretion processes onto the central compact object (Perna et al. 2006), but we offer here that the constancy of the $\delta t/t$ value of flares may partly be a by-product of the overall decay of the afterglow in so far as the sensitivity of the XRT to flares is naturally degraded as the overall flux level of the afterglow decays, thus *requiring* flares at later times (and hence, lower flux levels) to be longer in duration for enough counts to be collected to produce a significant flare seen above the background. Such a case can be seen in comparing the early-time flares in the first orbit of GRB 050713A to the flare seen in the third orbit. During the first orbit, the underlying flux level beneath the flares is poorly determined, but can be assumed to be 10–100 counts s^{-1} . We are dominated in this portion of the light curve by the Poissonian error in the flux, which in a 10 s integration will be 10–32 counts, or 3%–10%. Thus, for a flare to appear at the 6σ level above the background during this portion of the light curve, at most a 60% increase in fluence above the normal power-law decay is needed, which can be acquired in a few seconds by the introduction of a flare with twice the flux of the underlying afterglow. During the third orbit, however, the underlying afterglow flux level has dropped to ~ 0.1 counts s^{-1} . During a 10 s integration at 0.1 counts s^{-1} the Poisson error alone is 1 count, so for a flare to be detectable at 6σ above background at these count levels, the total fluence must be 6 counts, implying an increase in the rate from 0.1 to 0.6 counts s^{-1} during the 10 s interval, a sixfold increase, which has been seen only in the brighter flares. In order to be sensitive to the same 60% increase in flux level as during the first orbit, the flare that occurs at a flux level of 0.1 counts s^{-1} needs to have a Poisson error that is one-sixth of the total counts in the observation, i.e., 36 counts must be collected, which implies an exposure time of at least 180 s if produced by the introduction of a flare with twice the flux of the underlying afterglow. In other words, because the afterglow flux level decays as $t^{-\alpha}$, the exposure time needed to acquire the same fluence level increases as t^α . Thus, we see that in moving from the first orbit at $T_0 + 100$ s to the third orbit at $T_0 + 10,000$ s, assuming a typical underlying power-law decay of the afterglow of $\alpha \sim 1$, we have greatly decreased the temporal resolution of the XRT to detect flares (from a few seconds to a few hundred seconds). This is not to imply that there is not another more physical cause for the constancy of the $\delta t/t$ ratio seen in flares, but rather to note that the typical GRB seen by the *Swift* XRT does not provide sufficient flux at times typically

greater than a few ks to detect the shorter timescale flares that are so often seen during the first orbit.

In GRB 050713A, a hint of emission above the afterglow power-law decay appears in the XRT data at $T_0 + 45$ ks, although the statistics are, predictably, poor. This time is overlapped by *XMM-Newton* data, however, so we can look for evidence of a short flare in the *XMM-Newton* data at this time. In Figure 9 we show the *XMM-Newton* light curve, plotted linearly and zoomed near $T_0 + 45$ ks. Although a 1–2 σ deviation above the background decay is seen at $T_0 + 45$ ks, the *XMM-Newton* data appear consistent with a statistical fluctuation rather than a true flare similar to those seen earlier during the burst.

The presence of multiple flares in GRB 050713A argues against “one shot” emission mechanisms such as synchrotron self-Compton emission in a reverse shock or deceleration of the blast wave (Piro 2005a), and it argues in favor of a mechanism that can produce repeated flares, such as late-time central-engine activity. While it may remain possible that one of the several flares in GRB 050713A is due to the RS or the onset of the afterglow due to external shocks, the steep temporal decays of all the temporally fitted flares coupled with the photon indices of the flares (~ 1.25 – 2.5 ; Table 6) do not satisfy the closure relations of Sari et al. (1998), Chevalier & Li (1999), and Sari & Piran (1999) for propagation of the blast wave into either a wind or constant-density ISM. Together these points seem to argue in favor of an internal-shock origin for the flares seen in this burst.

3.3. Joint Spectral Fitting

Due to the relatively narrow spectral response function of the BAT (15–150 keV for mask-tagged events) and the XRT (0.3–10 keV), a spectral fit to data from only one of the two high-energy instruments on *Swift* is usually not able to discriminate between higher order spectral models. Analysts and authors are usually limited to choosing between a power-law or Band function. In GRB 050713A we have a rare case of data coverage overlap between BAT and XRT (0.3–150 keV) and also between BAT and K-W (15 keV to 14 MeV). Taking advantage of this where appropriate, considering the relative flux levels in the three instruments, we have jointly fitted spectral data sets between the two pairs of instruments. During the precursor and from $T_0 + 0$ to $T_0 + 16.5$ s, we perform joint fitting between BAT and K-W data. From $T_0 + 16.5$ to $T_0 + 78$ s we have only BAT data. From $T_0 + 78$ to $T_0 + 116$ s and during the onset of the flare at $T_0 + 160$ s we perform joint fitting between XRT and BAT. We have grouped the data into segments (as shown in Table 6) in order to temporally separate data that we expect may show significantly different spectral parameters. Segments 1–4 contain BAT and K-W data and are segmented to separate the precursor from the prompt-emission and the prompt-emission from the rapid-decay phase. Segment 5 contains BAT data only, and segments 6–10 contain XRT and BAT data. These are segmented to distinguish the three flares that have overlapping data and also to separate the rise of each flare from the decay of each flare. We attempt fits to each of these segments using four different spectral models: (1) an absorbed power law, (2) an absorbed cutoff or broken power law (cutoff for data extending beyond 150 keV, broken otherwise), (3) an absorbed Band function, and (4) an absorbed blackbody plus power law.

3.3.1. Segment 1: Precursor ($T_0 - 65$ to $T_0 - 55$ s)

The precursor is the most poorly sampled of all the regions. Despite the low number of counts in the region, a cutoff power law is favored over a single power law at 90% confidence according to the *F*-test. Of all the segments fit, the precursor has the

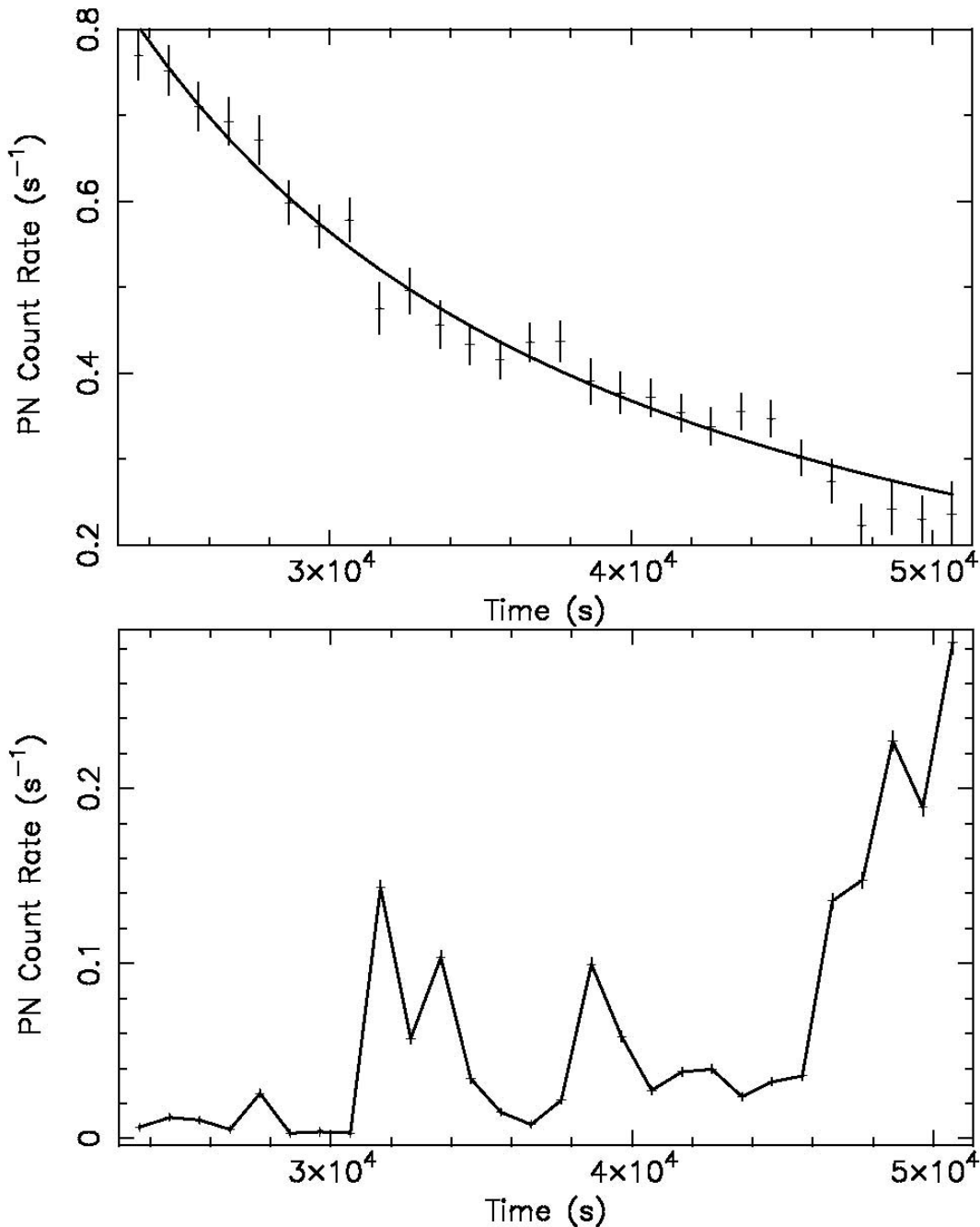


FIG. 9.—*XMM-Newton* light curves for the afterglow of GRB 050713A. The top panel shows the background-subtracted afterglow light curve for the PN detector. Crosses show the GRB source counts (1σ errors); the solid line shows the best-fit decay rate of $t^{-1.45}$. Time is plotted compared to the initial BAT trigger. The bottom panel shows the background light curve for the PN, normalized to the size of the source extraction region for comparison.

hardest photon index, regardless of the model that is used to perform the fits.

3.3.2. Segment 2: Prompt Emission Plateau ($T_0 + 0$ to $T_0 + 8.5$ s)

The plateau of the prompt emission is best fit by an exponentially cut off power law model with photon index = 1.26 and $E_{\text{peak}} = 421$ keV. Next to the precursor, the prompt plateau has the second hardest photon index of all segments fit, regardless of the model used.

3.3.3. Segment 3: Rapid Decay ($T_0 + 8.5$ to $T_0 + 25$ s)

As with the other data segments that contain K-W data, the rapid-decay segment is poorly fit by a simple power law and is

best fit by a cutoff power law or Band function. The photon index of the cutoff power law in segment 3 is quite similar to that in the prompt plateau, but the cutoff energy is somewhat lower (312 keV, compared to 421 keV in the plateau), suggesting that the highest energy flux is “shutting off” during the rapid-decay phase.

3.3.4. Segment 4: Plateau + Early Rapid Decay ($T_0 + 0$ to $T_0 + 16.5$ s)

This segment is an extension of the prompt segment to slightly later times, encompassing slightly more data. The cutoff power law or Band function is the best fit, with photon indices similar to segment 2 and E_{peak} between that in segments 2 and 3.

TABLE 6
GRB 050713A: JOINT SPECTRAL FITS

PARAMETER	SEGMENT									
	1 ($\delta t = -70$ to -49.5 s)	2 (0–8.5 s)	3 (8.5–25 s)	4 (0–16.5 s)	5 (59–68 s)	6 (68–95 s)	7 (100–113 s)	8 (113–150 s)	9 (159–171 s)	10 (171–200 s)
Power law:										
N_{H}	NA	NA	NA	NA	NA	0.52	0.59	0.60	0.54	0.38
Photon index.....	1.26	1.44	1.61	1.47	1.83	2.47	1.72	2.68	2.52	2.55
χ^2_{ν}	1.54	1.96	1.39	1.95	0.98	1.20	1.21	1.07	1.04	1.00
dof.....	12	101	91	98	26	74	98	125	22	37
Cutoff power law:										
Photon index.....	0.913	1.26	1.31	1.25	NA	NA	NA	NA	NA	NA
E_{peak}	270	421	312	400	NA	NA	NA	NA	NA	NA
χ^2_{ν}	1.20	1.60	1.02	1.29	NA	NA	NA	NA	NA	NA
dof.....	11	110	90	100	NA	NA	NA	NA	NA	NA
Broken power law:										
N_{H}	NA	NA	NA	NA	NA	0.58	0.43	0.45	NA	NA
Photon index 1.....	NA	NA	NA	NA	0.95	2.69	1.26	1.93	NA	NA
E_{break}	NA	NA	NA	NA	5.8	4.1	3.4	1.8	NA	NA
Photon index 2.....	NA	NA	NA	NA	2.1	1.5	2.0	2.8	NA	NA
χ^2_{ν}	NA	NA	NA	NA	1.06	1.31	1.03	1.04	NA	NA
dof.....	NA	NA	NA	NA	23	73	97	124	21	36
Band:										
N_{H}	NA	NA	NA	NA	NA	0.33	0.49	0.54	0.41	0.33
α	-1.13	-1.27	-1.27	-1.29	-2.01	-1.69	-1.46	-2.32	-1.98	-2.17
β	-1.26	-9.36	-2.39	-9.29	-9.07	-1.88	-9.36	-9.32	-9.04	-8.78
E_{peak}	101	761	244	636	994	10.6	30.7	10.6	10.6	10.6
χ^2_{ν}	1.85	1.61	1.03	1.28	1.06	2.11	1.11	1.13	1.26	1.12
dof.....	10	109	89	101	23	73	97	124	21	36
Power law + blackbody:										
N_{H}	NA	NA	NA	NA	NA	0.59	1.17	0.63	0.50	0.44
kT	3.59	59.4	26.4	44.97	NA	7.1	0.1	4.4	200	5.2
Blackbody norm.....	0.068	2.74	0.46	1.47	NA	0.07	2.48	0.01	2.90	0.01
Photon index.....	1.00	1.64	1.76	1.63	NA	2.75	2.00	2.77	2.43	2.83
Power-law norm.....	0.053	13.97	7.69	11.65	NA	1.53	2.32	2.03	0.51	0.44
χ^2_{ν}	1.15	1.79	1.03	1.60	NA	1.33	1.04	1.07	0.90	0.98
dof.....	10	109	89	101	NA	73	97	124	21	36

NOTES.— We group the data into segments to separate times that may show different spectra. Segments 1–4 contain BAT and K-W data and are segmented to separate the prompt-emission from the rapid-decay phase. Segment 5 contains BAT data only, and segments 6–10 contain XRT and BAT data. These are segmented to separate the rise and decay of each flare. We attempt fits to each segment using four spectral models: (1) an absorbed power law, (2) an absorbed cutoff or broken power law, (3) an absorbed Band function, and (4) an absorbed blackbody plus power law. In segments where a particular model was inapplicable or the fit did not converge, NA is entered in the table.

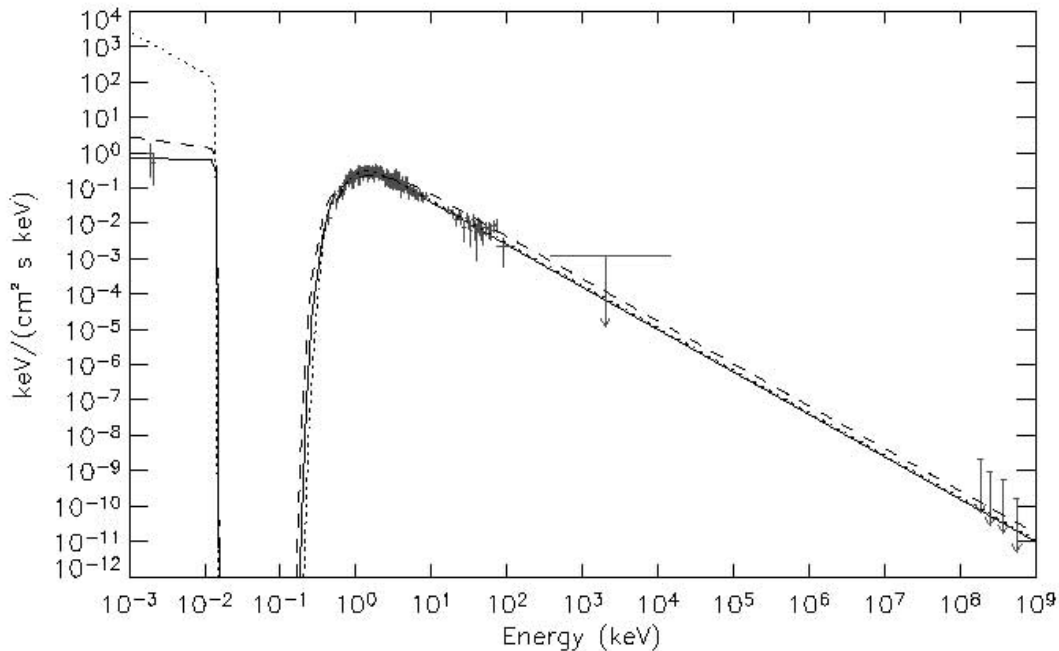


FIG. 10.—Combined multiplatform SED of the early afterglow of GRB 050713A from $T_0 + 20$ to $T_0 + 300$ s. Optical data are from RAPTOR-S at LANL and the Liverpool Robotic Telescope, soft X-ray (0.2–10 keV) data are from *Swift* XRT, hard X-ray (15–150 keV) data are from *Swift* BAT, and gamma-ray upper limits are from *Konus-Wind* (0.5–14 MeV) and MAGIC (175–500 GeV). The three lines plotted over the data represent the three models discussed as proposed fits to the SED in the text. The absorbed broken power law (solid line) is the only acceptable fit. The absorbed Band function (dashed line) and simple absorbed power law (dotted line) do not appear reconcilable with the data. The results suggest that the GRB flare emission is characterized by a single mechanism well represented by a broken power law, or that a more complex, possibly multicomponent emission mechanism is required to explain the complete SED. [See the electronic edition of the *Journal* for a color version of this figure.]

3.3.5. Segment 5: Rise of $T_0 + 60$ s Flare ($T_0 + 59$ to $T_0 + 68$ s)

This segment contains only BAT data and is included for completeness, although the narrowness of the BAT spectral response limits the ability to distinguish between models. A simple power law is a good fit with a photon index of 1.83. Here N_H is unconstrained. The power law plus blackbody model produces a good fit to this segment, but only with a very minimal blackbody component, effectively reproducing the fit of the simple absorbed power law. Therefore we consider the power law plus blackbody model inapplicable to this segment.

3.3.6. Segment 6: Decay of $T_0 + 60$ s Flare ($T_0 + 68$ to $T_0 + 95$ s)

Only in this segment, the data time ranges are mismatched between XRT and BAT (due to XRT observations beginning toward the end of the flare decay). Rather than ignore this flare or consider only the later part of the flare decay where XRT and BAT data coverage overlap, we have chosen to fit the entire BAT time range from $T_0 + 68$ to $T_0 + 95$ s, together with the $T_0 + 79$ to $T_0 + 95$ s XRT data (note that the Image Mode data taken at $T_0 + 73$ s are highly piled up and cannot be used spectrally), for consistency with our treatment of the other flares. A simple power law is a good fit to this segment, yielding $N_H = 5.2 \times 10^{21} \text{ cm}^{-2}$ and a photon index of 2.47, significantly softer than the rise of the flare, as expected.

3.3.7. Segment 7: Rise of $T_0 + 100$ s Flare ($T_0 + 100$ to $T_0 + 113$ s)

In the rise of the brightest flare seen in XRT, both an absorbed power law plus blackbody model and an absorbed broken power law model are significantly better fits (F -test probability 3×10^{-4}) than a simple absorbed power law. The power law plus blackbody

indicates $N_H = 1.2 \times 10^{22} \text{ cm}^{-2}$ and a relatively soft photon index of 2.0 with a blackbody temperature of $kT = 0.1$ keV. We note that this value of kT is below the XRT energy band and may therefore indicate a nonphysical spectral solution. The absorbed broken power law indicates $N_H = 4.3 \times 10^{21} \text{ cm}^{-2}$ and photon indices of $\Gamma_1 = 1.26$ and $\Gamma_2 = 2.01$, broken at 3.4 keV. These two models are somewhat degenerate in this data set, with both models producing a rollover in flux at low (below 0.5 keV) and high (above 50 keV) energies.

3.3.8. Segment 8: Decay of $T_0 + 100$ s Flare ($T_0 + 113$ to $T_0 + 150$ s)

The decay portion of this flare is well fit by a simple absorbed power law with $N_H = 6.0 \times 10^{21} \text{ cm}^{-2}$ and a photon index of 2.68. We note, however, that both an absorbed broken power law and absorbed power law plus blackbody are equally good fits to the data.

3.3.9. Segment 9: Rise of $T_0 + 160$ s Flare ($T_0 + 159$ to $T_0 + 171$ s)

The rise of the last flare with overlapping data is well fit by a simple absorbed power law with $N_H = 5.4 \times 10^{21} \text{ cm}^{-2}$ and photon index = 2.52; however, the absorbed power law plus blackbody is, strictly, a better fit according to the F -test, although only at about the 80% confidence level (F -test probability = 0.219), with $N_H = 5.0 \times 10^{21} \text{ cm}^{-2}$, $kT = 200$ keV, and a photon index of 2.43. We note that this value of kT is above the XRT-BAT energy band and may therefore indicate a nonphysical spectral solution.

3.3.10. Segment 10: Decay of $T_0 + 160$ s Flare ($T_0 + 171$ to $T_0 + 200$ s)

The decay of this flare is well fit by an absorbed power law with $N_H = 3.8 \times 10^{21} \text{ cm}^{-2}$ and a photon index of 2.55, although

TABLE 7
GRB 050713A: SED FIT DATA

Parameter	Value
Power law:	
N_{H}	$4.3 \times 10^{21} \text{ cm}^{-2}$
Photon index.....	2.14
χ^2_{ν}	10 (65 dof)
Broken power law:	
N_{H}	$(2.9 \pm 0.3) \times 10^{21} \text{ cm}^{-2}$
Photon index 1.....	1.1 ± 0.1
E_{break}	$1.3 \pm 0.2 \text{ keV}$
Photon index 2.....	2.2 ± 0.1
χ^2_{ν}	1.20 (63 dof)
Band:	
N_{H}	$(2.1 \times 10^{21}) \text{ cm}^{-2}$
α	-1.3
β	-2.2
E_{peak}	10.6 keV
χ^2_{ν}	2.97 (63 dof)

NOTES.—A broadband SED (R -band optical data points to 500 GeV upper limits) has been created, and we show the result of fits of three spectral models: (1) an absorbed power law, (2) an absorbed broken power law, and (3) an absorbed Band function. We do not report errors on the parameters in the power-law fit or Band function because these models are clearly unacceptable, as shown by the large values of χ^2_{ν} . Only the broken power law is an acceptable fit to the entire SED.

as with segment 9, the absorbed power law plus blackbody is also an acceptable fit with $N_{\text{H}} = 4.4 \times 10^{21} \text{ cm}^{-2}$, $kT = 5.2 \text{ keV}$, and a photon index of 2.83. It should be noted that the BAT flux is very near the noise level in this segment and really provides only an upper limit on the spectral-fitting process in the higher energy region.

3.4. Broadband SED

We have produced the broadband SED (spectral energy distribution) of the afterglow of GRB 050713A over the time range from $T_0 + 20$ to $T_0 + 300 \text{ s}$ (Fig. 10). This time range includes detections of the burst afterglow in the optical from the RAPTOR-S and Liverpool telescopes (corrected for the Galactic extinction in this direction of $A_R = 1.04$ [Schlegel et al. 1998]) and in the X-ray from *Swift* BAT and XRT. It also includes upper limits in the gamma-ray energy range from K-W (whose detectable emission ends at $T_0 + \sim 10 \text{ s}$) and in the GeV energy range from MAGIC. A similar SED has been addressed by the MAGIC collaboration in their paper regarding the MAGIC flux upper limit (Albert et al. 2006), in which they note that the SED composed of data from *Swift* and MAGIC (0.2 keV to 400 GeV) is fit by a Band function at low energy and that the MAGIC data are consistent with a single unbroken power law extending from E_{peak} (at $\sim 400 \text{ keV}$) to the MAGIC limits up to 500 GeV. We confirm this result, citing a best-fit photon index for a single-power-law fit from 400 keV to 500 GeV of $\Gamma = 2.1 \pm 0.1$ and a reduced $\chi^2_{\nu} = 1.66$ for 63 dof. We further note that in performing our fit to the MAGIC data, we have treated the MAGIC upper limits as data points during our fit and thus that our photon index of 2.1 is only a lower limit on the true photon index of a power law that would fit the true flux level at GeV energies. Our results here are, therefore, consistent with the analysis of the Albert et al. in which they show that their data are consistent with a power-law photon index of 2.5 from 400 keV to 500 GeV.

We add that a Band function fit is not, however, consistent with the data when we also consider the contemporaneous optical detections. The relative faintness of the optical detections

compared to the X-ray detections combined with the upper limits from K-W and MAGIC requires an absorbed broken power law fit. Figure 10 shows the best fit to the entire SED using an absorbed power law (*dotted line*), absorbed broken power law (*solid line*), and absorbed Band function (*dashed line*). The spectral parameters and fit characteristics for each of these fits are shown in Table 7. We have not corrected for the attenuation of flux above 10 GeV due to photon-photon interactions with the infrared background (de Jager & Stecker 2002; Kneiske et al. 2004; Primack et al. 2005); however, our spectral-fit results will remain valid independent of this effect due to the constraints placed by the K-W limiting flux measurement from 20 keV to 14 MeV.

4. SUMMARY

GRB 050713A is one of the rare bursts observed simultaneously in soft X-rays (XRT), hard X-rays (BAT), and gamma rays (K-W). The broad spectral coverage of these simultaneous measurements has allowed us to fit the early prompt emission, rapid decay, and several flares in the early emission with several different spectral models. In general, we find a cutoff-power-law model to be a good fit to segments with data extending into the MeV range, and are thus able to constrain the high-energy component of the model. For data segments with 0.3–150 keV coverage (BAT and XRT data), we find that a simple absorbed power law is often an adequate fit to the data, although an absorbed power law plus blackbody or absorbed broken power law model seems to sometimes be a marginally better fit during periods of flaring activity.

The light-curve structure of GRB 050713A is quite typical of many GRBs that have been observed by *Swift*. It has an early section showing steep decay slopes of $\alpha > 5$ and bright flares extending until $T_0 + \sim 1 \text{ ks}$, followed by a break to a flatter section with decay slope $\alpha \sim 1.0$ lasting until $T_0 + \sim 25 \text{ ks}$, followed by a break to a steeper slope of $\alpha = 1.45$.

We have temporally separated the early, flaring portion of the burst into 10 segments and attempted to fit each segment using four different spectral models: (1) an absorbed power law, (2) an absorbed cutoff or broken power law (cutoff for data extending beyond 150 keV, broken otherwise), (3) an absorbed Band function, and (4) an absorbed blackbody plus power law. In all segments where at least two instruments provide significant, simultaneous levels of emission, and hence the spectral data span more than 2 decades in energy, we find that at least one of the higher order spectral models is acceptable and, in several cases, is a better fit to the data than a simple absorbed power law. This suggests that the spectral shape of GRB flares, while consistent with a simple absorbed power law when viewed through any particular narrow spectral window, is intrinsically fit in the broadband by a model with attenuated flux above (and possibly below) some threshold energy.

It has long been known that GRB prompt emission is better fit by spectral models with a high (and sometimes low) energy cutoff than by a simple absorbed power law (Ryde 2005; Band et al. 1993), and thus the indication that GRB flares are fit by a similar spectral model suggests that similar emission mechanisms may be responsible for the production of flares and for the prompt emission itself, namely, internal shocks produced as a result of central-engine activity. Since the discovery of X-ray flares in GRBs by *Swift*, relatively few of the flares have been observed simultaneously across a broad enough energy range to determine whether such higher order models are necessary to fit their spectra, making the multi-instrument observations of GRB 050713A unique and valuable.

We have also examined the temporal properties of the flares seen in GRB 050713A as early as $T_0 + 80 \text{ s}$ and as late as

$T_0 + 10$ ks. In all cases we find the flares to have steep power-law rise and decay slopes and $0.1 < \delta t/t < 1$, which also suggests internal rather than external shocks as the production mechanism for the flares (Burrows et al. 2005b; Ioka et al. 2005). We have noted that the presence of multiple flares and the failure of those flares to fit the closure relations associated with the external shock in a wind or constant-density ISM further argues in favor of the internal-shock origin for the flares.

We have furthermore discussed the difficulty that *Swift* XRT will face in detecting late-time flaring activity. We have noted that the XRT will have difficulty resolving late, short-timescale flares due to the low XRT count rates typically involved. Data from higher throughput instruments such as *XMM-Newton* EPIC will be important for constraining flares at these times. GRB 050713A has simultaneous coverage at moderately late times with *XMM-Newton* EPIC, but no conclusive evidence of flaring in the *XMM-Newton* data has been found in this case.

Finally, we have created a broadband SED of the flaring region of GRB 050713A from 0.002 keV to 500 GeV at times from $T_0 + 20$ to $T_0 + 300$ s. We find that the SED is inconsistent with

a single absorbed power law or an absorbed Band function and is best fit by an absorbed broken power law. This overall SED again implies that GRB flares are best fit by a spectral model similar to that of the prompt emission itself and thus suggests a common mechanism for the emission from the prompt phase and from flares.

This work is supported at Penn State by NASA contract NAS5-00136. We gratefully acknowledge the contributions of dozens of members of the *Swift* team at Penn State, the University of Leicester, OAB, GSFC, ASDC, MPE, and our sub-contractors, who helped make this observatory possible, and we are grateful to the Flight Operations Team for their support above and beyond the call of duty. This work contains observations obtained with *XMM-Newton*, an ESA science mission with instruments and contributions directly funded by ESA member states and the USA (NASA). The K-W experiment is supported by Russian Space Agency contract and RFBR grant 06-02-16070.

REFERENCES

- Albert, J., et al. 2006, *ApJ*, 641, L9
 Aptekar, R. L., et al. 1995, *Space Sci. Rev.*, 71, 265
 Band, D., et al. 1993, *ApJ*, 413, 281
 Barthelmy, S., et al. 2005a, *Space Sci. Rev.*, 120, 143
 ———. 2005b, *Nature*, 438, 994
 Burrows, D. N., et al. 2005a, *Space Sci. Rev.*, 120, 165
 ———. 2005b, *Science*, 309, 1833
 Chevalier, R. A., & Li, Z. Y. 1999, *ApJ*, 520, L29
 de Jager, O. C., & Stecker, F. W. 2002, *ApJ*, 566, 738
 Falcone, A. D., et al. 2005, *GCN Circ.* 3581, <http://gcn.gsfc.nasa.gov/gcn/gcn3/3581.gcn3>
 ———. 2006, *ApJ*, 641, 1010
 Gallant, Y. A., et al. 1999, *A&AS*, 138, 549
 Gehrels, N., et al. 2004, *ApJ*, 611, 1005
 Gendre, B., et al. 2007, *A&A*, in press (astro-ph/0603431)
 Hill, J. E., et al. 2004, *Proc. SPIE*, 5165, 217
 ———. 2006, *ApJ*, 639, 303
 Ioka, K., et al. 2005, *ApJ*, 631, 429
 Kneiske, T. M., et al. 2004, *A&A*, 413, 807
 Kobayashi, S., et al. 2007, *ApJ*, in press (astro-ph/0506157)
 Malesani, D., et al. 2005, *GCN Circ.* 3582, <http://gcn.gsfc.nasa.gov/gcn/gcn3/3582.gcn3>
 Mirzoyan, R., et al. 2005, in *Proc. 29th Int. Cosmic Ray Conf. (Pune)*, 4, 23
 Nousek, J. A., et al. 2006, *ApJ*, 642, 389
 Palmer, D. M., et al. 2005, *GCN Circ.* 3597, <http://gcn.gsfc.nasa.gov/gcn/gcn3/3597.gcn3>
 Perna, R., Armitage, P. J., & Zhang, B. 2006, *ApJ*, 636, L29
 Piro, L. 2005a, *ApJ*, 623, 314
 ———. 2005b, *Nuovo Cimento C*, 28, 473
 Primack, J. R., Bullock, J. S., & Somerville, R. S. 2005, in *AIP Conf. Proc.* 745, *International Symposium on High Energy Gamma-Ray Astronomy*, ed. F. A. Aharonian et al. (New York: AIP), 23
 Romano, P., et al. 2006, *A&A*, 450, 59
 Ryde, F. 2005, *ApJ*, 625, L95
 Sari, R., & Piran, T. 1999, *ApJ*, 520, 641
 Sari, R., et al. 1998, *ApJ*, 497, L17
 Schlegel, D. J., Finkbeiner, D. P., & Davies, M. 1998, *ApJ*, 500, 525
 Wren, J., et al. 2005, *GCN Circ.* 3604, <http://gcn.gsfc.nasa.gov/gcn/gcn3/3604.gcn3>
 Zhang, B., & Mészáros, P. 2004, *Int. J. Mod. Phys. A*, 19, 2385
 Zhang, B., et al. 2006, *ApJ*, 642, 354